DFT Mechanistic Investigation of an Enantioselective Tsuji–Trost Allylation Reaction

By: Kate E. McPherson, Mitchell P. Croatt, Andrew T. Morehead, Jr., and Andrew L. Sargent

Reprinted with permission from:

"DFT Mechanistic Investigation of an Enantioselective Tsuji-Trost Allylation Reaction" Kate E. McPherson, Mitchell P. Croatt, Andrew T. Morehead, Jr., and Andrew L. Sargent
Organometallics 2018, 37, 3791-3802.
https://pubs.acs.org/doi/full/10.1021/acs.organomet.8b00507

Abstract:

A comprehensive mechanistic examination of an asymmetric palladium-catalyzed Tsuji–Trost allylation reaction that identifies the enantioselective step was completed utilizing DFT computational tools and the nudged elastic band method. Key components of the study include (a) plausible reaction pathways for the full interconversion of a square-planar palladium allyl enolate intermediate with low barriers relative to the subsequent enantioselectivity-determining reductive C–C coupling step, thereby disputing the previously identified mechanism, (b) a detailed analysis of the factors influencing the stereochemical control involved in forming the preferred configuration via the reductive C–C coupling step, (c) a comprehensive examination of the competing outer-sphere mechanism that includes a metal counterion as an escort to the nucleophile in order to modulate the effects of modeling the reaction step of oppositely charged species, and (d) examination of the possible role water plays in stabilizing a keto-coordinated adduct of PdII-η1-allyl, formed early in the catalytic cycle, relative to a carboxylate-coordinated adduct, the known resting state of the reaction. Barrier energies for the enantioselective C–C coupling are investigated with several levels of theory, and together they support a reaction mechanism consistent with the preferred formation of the correct enantiomer on the basis of the enantiomer of the ligand selected.

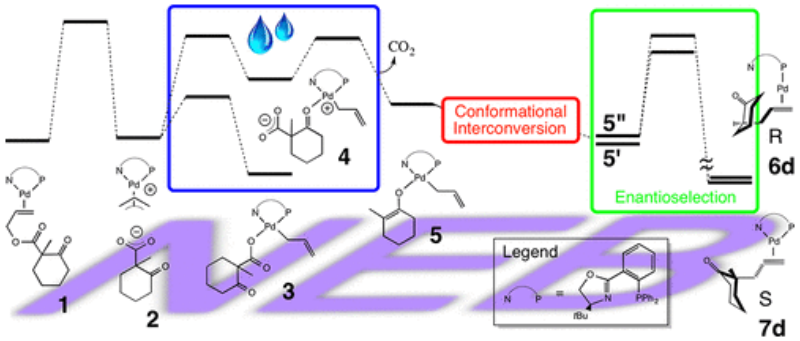

Keywords: Tsuji–Trost allylation reaction | DFT

Article:

Introduction

As the worldwide demand for chiral, enantioenriched chemicals increases, the interest in and development of enantioselective catalysis will continue to grow.(1) Two processes that are of particular value, due to the difficulty and complexity generated, are reactions that form C–C bonds and reactions that form quaternary centers. The palladium-catalyzed decarboxylative allylation reaction not only allows for formation of a C–C bond at a quaternary carbon but also does so in an enantioselective manner using simple, readily available starting materials.(2−4) The molecular complexity generated in this process has enabled the enantioselective and step-economical(5) synthesis of many molecules including elatol,(6) mycophenolic acid,(7) aspidospermine,(8,9) guttiferone A,(10) folicanthine,(11) martinellic acid,(12) and the Kopsia indole alkaloids.(13) The incredible value of this reaction provided the inspiration to study it in a more in-depth manner.

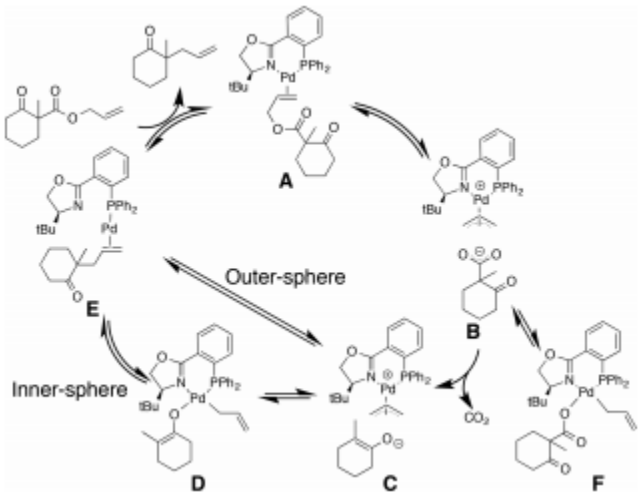

Scheme 1. Basic Mechanism

Refinement and optimization of the catalytic, enantioselective process requires a detailed understanding of the reaction mechanism, which allows the rational design of new ligands and clarifies the role of additives. For the case of palladium-catalyzed decarboxylative allylic alkylation reactions, the reaction examined herein, the efficiency and enantioselectivity vary depending on the nature of the associated nucleophile and electrophile, along with the ligands on the palladium catalyst.

The basic mechanism for the decarboxylative allylation is shown in Scheme 1. Following coordination of the substrate to form **A**, oxidative addition forms ion pair **B**. Intermediate **B** is in equilibrium with complex **F**, which is the resting state of the catalytic cycle. Irreversible decarboxylation from **B** leads to **C**. Intermediate **C** is a key branch point, as either coordination forming **D** and subsequent inner-sphere reductive elimination generates **E** or direct outer-sphere nucleophilic attack leads to **E** as well. This is a critical juncture in terms of catalyst design, as the steps that produce enantioselection purportedly reside in this part of the mechanism. Ligand exchange then closes the catalytic cycle.

Several previous computational mechanistic studies have investigated allylic alkylation reactions that support an outer-sphere nucleophilic attack pathway.(14) Facilitating the outer-sphere mechanism in these cases is the presence of a labile counteranion such as a halide.

Coordination of the halide to the cationic metal center renders it formally neutral, thereby moderating the interaction between it and the attendant nucleophile such that it is no longer dominated by the electrostatic attraction of the ion pair. A recently reported enantioselective Tsuji–Trost allylation reaction of an allyl enol carbonate to form an α-allylated ketone with a quaternary stereocenter differed in that no additional counteranion was present.(2) The associated computational mechanistic analysis therefore examined both outer- and inner-sphere pathways.(15,16) Due to the length and complexity of the mechanism, the study focused primarily on the steps following the decarboxylation (i.e., the **C** → **E** step(s)) and not only established a preference for an inner-sphere pathway but also stated that the probable enantiodetermining step involved rearrangement from a square-pyramidal Pd(II) variant of **C** with an η3-allyl and apical enolate to a square-planar Pd(II) complex with an η1-allyl (**D**). Facile rearrangement of the latter complex was acknowledged to potentially weaken this model of enantioselection, but no examination of those pathways was presented, presumably due to the time-consuming, difficult calculations that would be required using standard computational techniques.

In the present study, the allylation reaction of the allyl enol carbonate is re-examined with particular attention paid to four features that were not explored in the prior study: (1) the energetics of conformational rearrangement within the square-planar Pd(II) allyl enolates **D**, (2) the enantioselective reductive C–C coupling step from the consequent isomers of **D**, (3) systematic examination of the various outer-sphere reaction pathways with a metal ion escorted nucleophile, and (4) the important role of trace water and its effect on decarboxylation. Routine density functional theory (DFT) computational tools are used along with the emerging nudged elastic band (NEB) methods for mapping the reaction minimum energy pathways, and the results provide a more detailed mechanism for this important reaction. We have previously demonstrated the utility of the NEB method in providing critical reaction energy path information in complex organometallic transformations,(17) and the analysis reported herein reinforces this conclusion.

Computational methods

DFT methods were employed from the G09(18) package to evaluate the molecular energies, equilibrium geometries, and vibrational frequencies. In-house versions of the NEB(19) and improved dimer(20,21) methods were used to traverse reaction pathways and locate transition states. Routine calculations involved the B3LYP(22,23) hybrid exchange correlation functional, a 6-31g* basis set for the nonmetal atoms and a def2-tzvp(24) basis for palladium, and solvation corrections from the polarized continuum model (pcm)(25,26) with the THF dielectric constant in the universal implicit solvent model (SMD).(27) NEB calculations utilized 19 images (17 movable) and were typically run for a few hundred cycles before the climbing image option(28) was activated for another few hundred cycles. Occasionally, the NEB calculations would converge, but more commonly, the highest-energy image and either an adjacent image or the tangent vector to the NEB minimum energy path was entered into the improved dimer program to refine the transition state. Certain steps of the catalytic cycle required NEB images to be created depicting asynchronous atomic movement, such as in the case of the reductive C–C coupling step. In this step, standard molecule building software was used to bring the η1-allyl and enolate fragments in close proximity where C–C coupling could begin. An image representing this structural relationship was used as the central point in the set

of NEB images; nine interpolated images preceded it, and nine followed. A test on this step with NEB images derived from standard interpolation of reactants and products found that NEB would eventually arrive at a pathway that was asynchronous, but it required over 1300 cycles, which is prohibitively resource and time intensive. All stationary points were verified through frequency calculations. Additional levels of theory were examined to gauge the effect of a larger basis set (6-31+g**), alternate solvent dielectric (H2O), dispersion interactions (via the m062x(29) functional), and different solvent model (COSMO(30−32)) on the reaction structures and energetics. In all cases, full geometry optimizations, reaction paths, transition states, and frequency calculations were recalculated at the different levels of theory to evaluate the full effect.

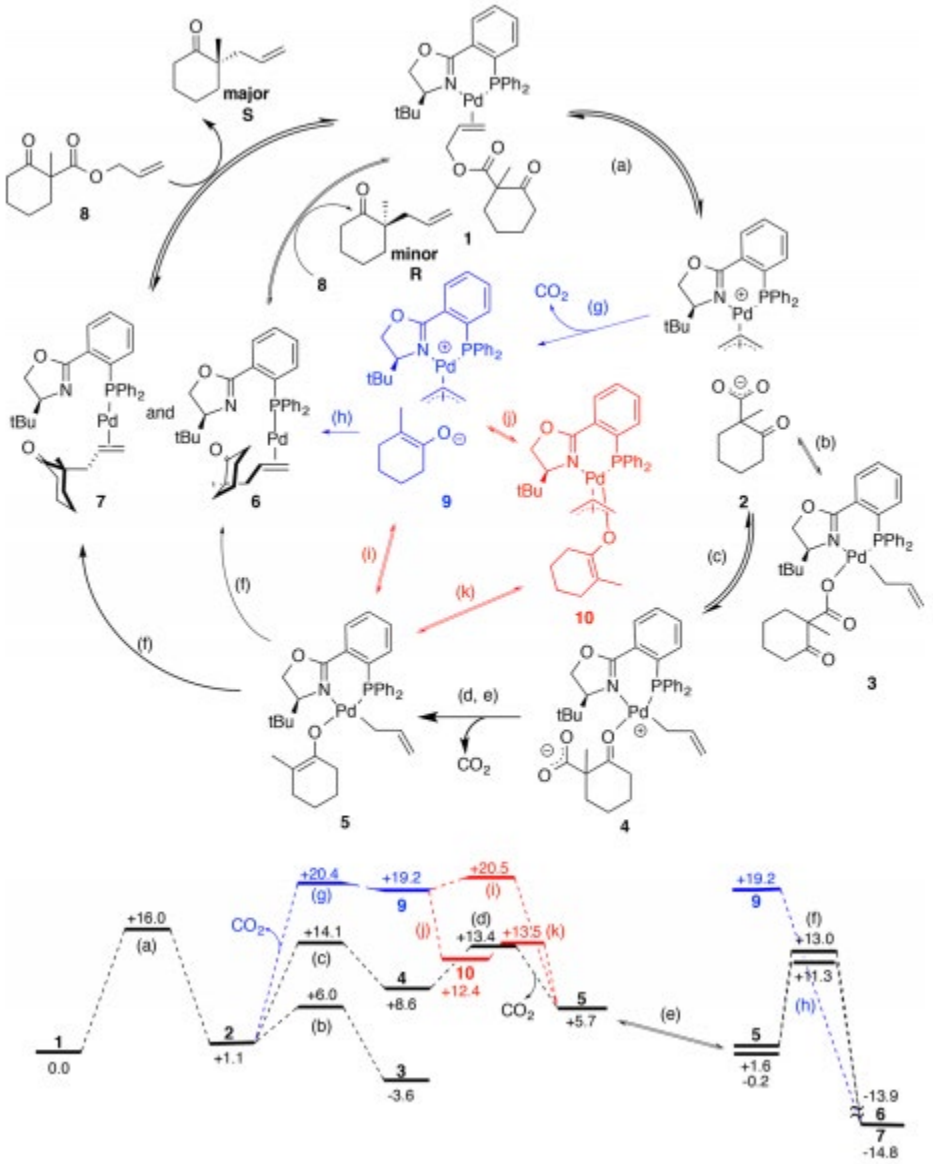

Scheme 2. Proposed Mechanism and Reaction Energy Path

Results and Discussion

Our comprehensive examination of the catalytic cycle, shown in Scheme 2, reveals important details about the mechanism that have been previously unexplored. The catalytic cycle itself is drawn in black, and the bold arrows indicate the major pathways. The blue and red pathways will be included in the discussion, as they constitute the outer-sphere pathway and the recently reported enantioselective step,(15,16) respectively, both of which were found in this study to be less energetically favorable. Initial coordination of a β-keto ester substrate (8) to the Pd(0) center results in a three-coordinate complex (1) that represents the active catalyst and the energetic baseline in the reaction energy path. The three-coordinate complex undergoes an intramolecular nucleophilic attack style oxidative addition (a) to form 2, whereby two electrons from the palladium–alkene complex attack the antibonding C–O orbital of the ester substrate to form an η3-allyl and displace the β-keto carboxylate, forming a tight ion pair. The calculated barrier for this oxidative addition step is +16.0 kcal/mol.

Recombination of the cation/anion pair along with decarboxylation forms complex 5, and the details of the corresponding pathways that evolve through complexes 3, 4, 9, and 10 will be discussed in detail below. Complex 10 (which can be accessed via the decarboxylation of 2 or the rearrangement of 5) was previously proposed and calculated to be a five-coordinate square-pyramidal complex with the enolate oxygen in the apical site. The previous study by Goddard proposed that 10's rearrangement to 5 was the enantioselective step of the reaction.(16) Since there are many possible isomers of 5 (vide infra), it is critical to know the energetics of the different structures and the transition states between them. If the interconversion between these isomers is more rapid than reductive elimination, the enantioselective step must be the reductive elimination and cannot come earlier in the catalytic cycle.

Three fundamental ligand rearrangements interconvert the conformers of 5 capable of reductive elimination in an energetically accessible manner: (a) η1-allyl rotation about the sp3–sp2 C–C bond, (b) enolate half-chair to half-chair interconversion, and (c) enolate rotation about the O–C bond, as shown in Figure 1. From the two simple conformers formed by each of these three ligand rearrangement processes, a total of eight principal conformational isomers (2 × 2 × 2) that can reductively eliminate are possible. Figure 2 illustrates these eight conformers in structures 5a,g,j,p,q,u,x,ab, along with the corresponding calculated energetics for each. The distinguishing feature of these eight conformers is that, with a single exception (structure 5o, to be discussed below in more detail as part of the analysis of the enantioselectivity), they constitute the lowest energy species that also retain the allyl and enolate in relative proximity such that their structural evolution en route to the C–C coupled products does not traverse additional conformational minima. While any of the conformers shown in Figure 2 could potentially undergo reductive elimination, those that require significant rearrangement in order to appropriately position the allyl and enolate to couple result in substantially higher barriers.

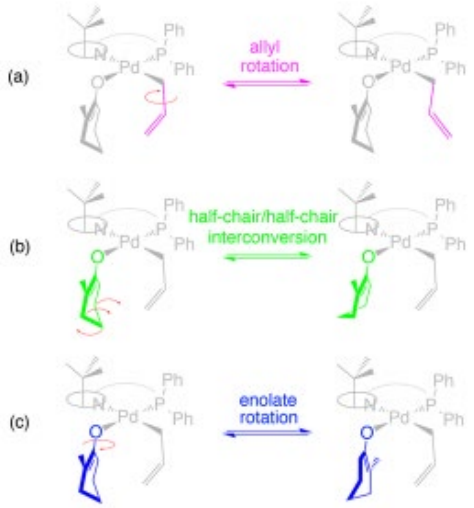

Figure 1. Fundamental ligand rearrangement motions involved in the conformational interconversion of 5 including (a) η1-allyl rotation about the sp3−sp2 C−C bond, (b) half-chair/half-chair interconversion, and (c) enolate rotation about the O−C bond. Color coding matches the corresponding ligand motions in Figure 2.

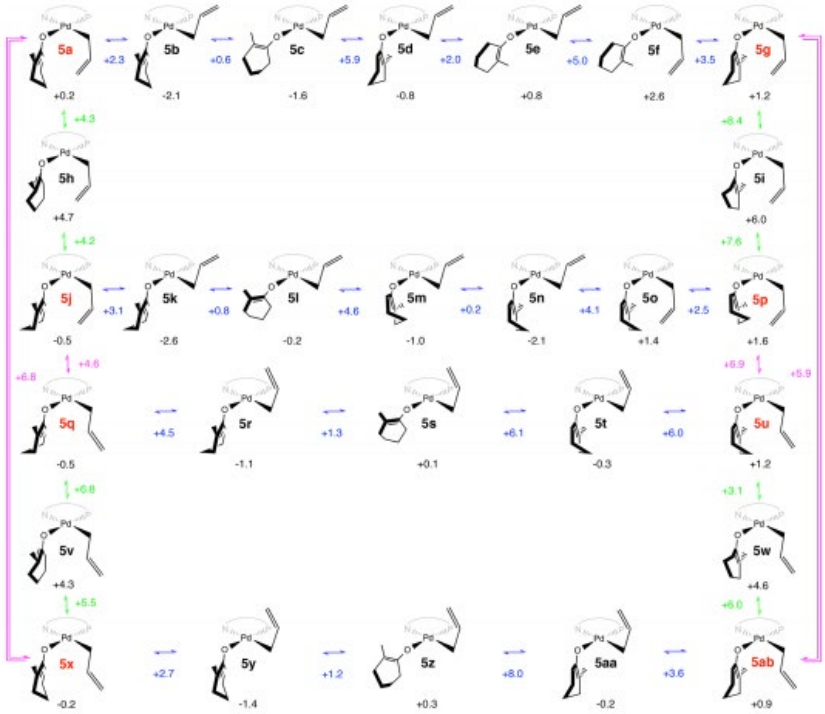

Figure 2. Plausible interconversion pathways between eight conformers of the Pd(II) enolate η1 allyl complex. Gibbs solvation free energies are given below each structure in black. Gibbs solvation free energies of activation are given adjacent to each reaction arrow connecting neighboring minima and are color coded in accord with the three fundamental ligand motions shown in Figure 1, with allyl rotation in purple, enolate half-chair/half-chair interconversion in green, and enolate rotation about the O−C bond in blue. The eight conformers that most likely

undergo reductive elimination are labeled in red. All energies are reported relative to 1, the purported overall baseline of the catalytic cycle, for simplicity, in units of kcal/mol.

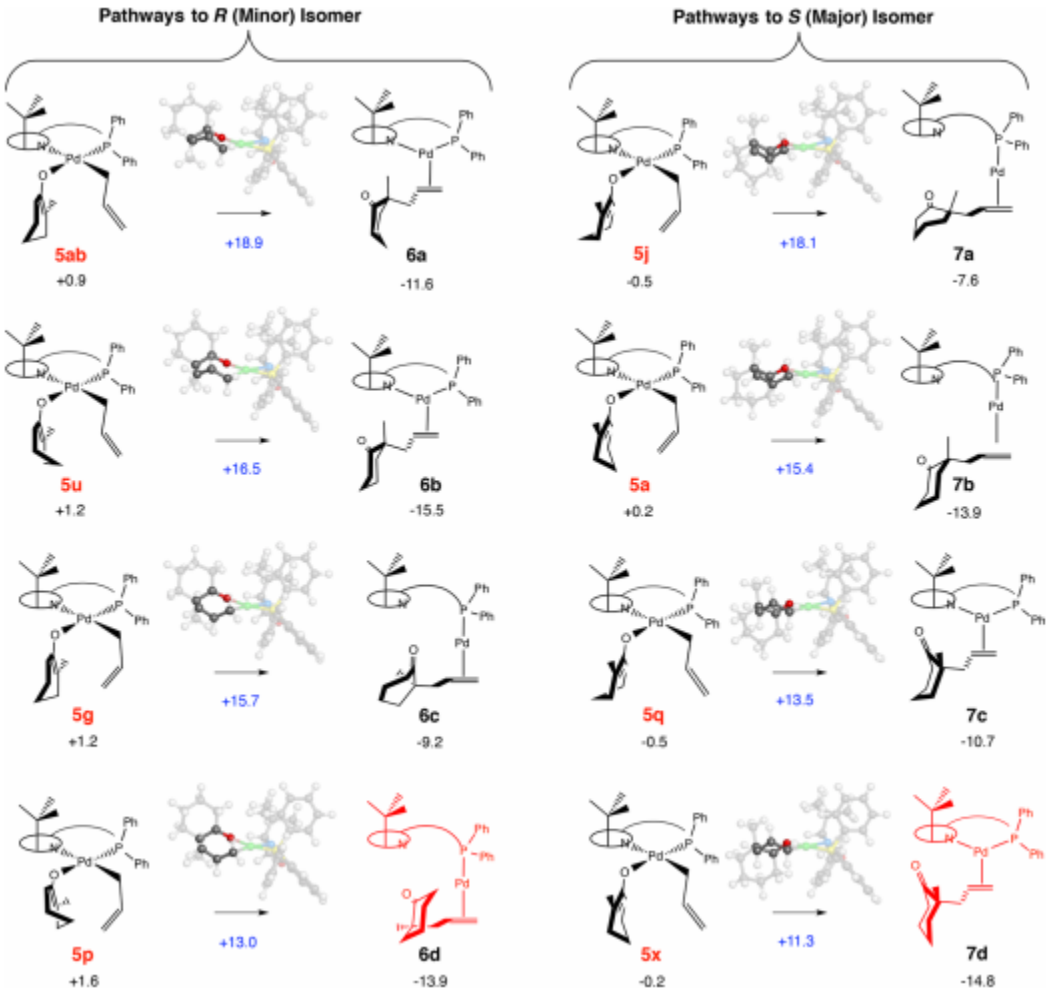

Figure 3. Reductive C−C coupling from eight Pd(II) allyl-enolate isomers, arranged by similar type leading to R (structures 6) and S (structures 7) enantiomers in each row of the figure. 3D molecular structures of the associated transition states are shown above the reaction arrows, and the highlighted atoms reveal the boat or chair conformations of the atoms involved in coupling. Gibbs solvation free energies are given in black, while the corresponding solvation free energies of activation are shown in blue. All values are reported in kcal/mol relative to baseline 1.

The difference in solvation free energies between all eight principal conformers is 2.1 kcal/mol; the two extremes come from structures 5j (or 5q) and 5p with values of −0.5 and +1.6 kcal/mol. Utilizing the NEB method, we identified pathways connecting these conformers via a total of 28 structural minima associated with the interconversion process, and these are shown in Figure 2. Certainly, other pathways that connect these and/or different intermediates are possible, but the pathways shown in Figure 2 allow for the complete low-energy interconversion of the principal Pd(II) allyl-enolate isomers, and a more detailed description of these pathways follows.

Rotation about the sp3–sp2 C–C bond of the η1-allyl is a direct, single-step event and is denoted in Figure 2 by the purple arrows and corresponding purple free energies of activation

(steps 5a–5x, 5j–5q, 5g–5ab, and 5p–5u). The two conformers differ in the orientation of the double bond; in one instance the CH2 is pointing inward toward the enolate, and in the other it is pointing outward toward the diphenylphosphino group of the ligand.

Interconversion of the two half-chair conformations of the enolate pass through a flattened "chair-like" intermediate, and these transformations are depicted in green in Figure 2 (steps 5a–5h–5j, 5g–5i–5p, 5q–5v–5x, and 5u–5w–5ab) where structures 5h,i,v,w are the flattened "chair-like" intermediates.

The most complex motions, involving three to five intermediates, reside in the low-energy pathways connecting the enolate rotamers. These transformations are denoted by the blue arrows and energies in Figure 2 (steps 5a–5b–5c–5d–5e–5f–5g, 5j–5k–5l–5m–5n–5o–5p, 5q–5r–5s–5t–5u, and 5x–5y–5z–5aa–5ab). Direct, single-step enolate rotation is a relatively high energy event, with solvation free energies of activation of 14.6, 16.7, 15.0, and 16.6 kcal/mol for the rotations converting 5a–5g, 5j–5p, 5q–5u, and 5x–5ab of Figure 2, respectively. The steric constraints of the ligand, however, require two additional types of motion along with the rotation in order to yield lower overall pathways and include η1-allyl rotation about the Pd–C bond and a rocking motion of the enolate. These multistep enolate rotation pathways are significantly lower in energy (the highest barrier is 8.0 kcal/mol) than the direct rotations mentioned above.

Conformer 5k is the lowest energy minimum in the interconversion process, with a solvation free energy of −2.6 kcal/mol relative to 1. With the irreversible decarboxylation step completed, subsequent barrier heights could be evaluated relative to structure 5k, as this intermediate is effectively the resting state for the interconversion and reductive elimination processes. To ease comparison with the earlier steps, however, the relative energies will continue to be reported relative to compound 1.

Of the 32 barriers depicted in Figure 2, the highest solvation free energy of activation is 11.0 kcal/mol higher in energy than 5k (8.4 kcal/mol higher than 1). The barrier heights for interconversion among any of these conformers is significantly lower than those leading to reductive C–C coupling, with the lowest barrier for the coupling being +13.9 kcal/mol relative to 5k (+11.3 kcal/mol relative to 1). The plausible pathways for the full interconversion process illustrated in Figure 2 therefore provide support for rapid pre-equilibration among all eight conformers of the Pd(II) enolate η1-allyl complex prior to the reductive C–C coupling step. These critical data indicate that the enantiodetermining step is the reductive C–C coupling step, not the square- pyramidal to square-planar rearrangement process.

As mentioned in Computational Methods, reductive C–C coupling pathways from the isomers of 5 are particularly problematic to calculate using traditional methods, since a significant amount of atomic rearrangement takes place in an asynchronous manner. Synchronous transit guesses of transition states generate structures that are poor estimates of the C–C coupling saddle points. NEB calculations that utilized asynchronous atomic movement which first allowed enolate-allyl proximal approach followed by the subsequent transformation from four-coordinate Pd(II) to two- or three-coordinate Pd(0) allowed us to readily locate transition states for reductive coupling from the eight relevant conformers of 5 (5a,g,j,p,q,u,x,ab) shown in Figure 3.

The reductive C–C coupling can proceed with reasonable barriers from any of the eight conformers shown in Figure 3 and evolves through a seven-membered metallacyclic transition state. Careful analysis of the figure reveals that two features within the complex dictate the height of the reductive C–C coupling barrier. The primary feature is the orientation of the allyl

group relative to the enolate, and the secondary feature is whether the six-membered ring of the enolate will end up in the chair or boat conformation as a result of the coupling step.

At the transition state, where the C–C bond is formed, if the enolate and allyl groups are oriented such that the atoms associated with the coupling event (see highlighted atoms in the 3D TS structures of Figure 3) adopt a chair conformation, then the coupling barrier is lower. This is the case for steps 5p–6d, 5x–7d, 5g–6c, and 5q–7c. If the corresponding atoms of the enolate and allyl groups are oriented instead in a boat conformation, then the coupling barrier is higher. This is the case for steps 5u–6b, 5a–7b, 5ab–6a, and 5j–7a.

Among all pathways, the secondary distinguishing feature involves whether the half-chair of the enolate is disposed such that during the C–C coupling the six-membered ring will finish in the chair or boat conformation, respectively. Within a given enolate-allyl orientation (i.e., the orientation at the transition state that adopts a chair or boat conformation during the coupling) the lowest energy pathway is that which leads to the chair conformation for the cyclohexanone. For example, note that steps 5p–6d and 5x–7d, which proceed through a chair transition state for the coupling, and 5u–6b and 5a–7b, which proceed through the boat transition state, all result in the chair conformation of cyclohexanone. These four couplings are lower energy than the respective steps 5g–6c and 5q–7c, and 5ab–6a and 5j–7a, which result in the boat conformation of cyclohexanone.

The origin of the energetic differences between the reductive coupling from 5x and 5p that determines the enantioselection is a complex combination of factors. As shown in Figure 4, the immediate visual impression is that the interaction of the methylene of the enolate and the ligand t-Bu group (circled in red) must determine the energetic difference (and favors the formation of enantiomer S). In this context it is helpful to examine reductive elimination from 5o also, a conformer where the enolate is rotated down and is spatially more distant from the t-Bu group. To investigate the role that the steric interactions between the t-Bu substituent and the substrate play, we examined the coupling reaction for complexes 5x,p,o, where the t-Bu substituent was replaced with a methyl or hydrogen. Note that, even with a hydrogen substituent, the ligand possesses a helical relationship between the two phenyls on the diphenylphosphino group that makes the top and bottom of the ligand slightly different, though this difference is small enough that it does not affect the barriers for the reductive elimination. The relevant calculated energies and transition state bond distances for the associated couplings are contained in Table 1. Note that there is a difference between the geometry of 6d dependent on the R group: for the t-Bu group, the geometry is linear (divalent), while for the smaller methyl and hydrogen R groups, the geometry retains the chelate and is trigonal. The difference can be attributed to the steric bulk of the t-Bu group, which interacts with the bound product and dissociates the oxazoline.

Figure 4. Space-filling structural models of the transition state structures for 5x → 7d, 5p → 6d, and 5o → 6d. The red oval highlights the steric interaction of the enolate methylene and the ligand t-Bu. The numbered atoms P1−Pd2−C3−C4 are used to define thedihedral angles given in Table 1.

	5x → 7d						5p → 6d						5o → 6d					
	5x	5x → 7d transition state					5p	5p → 6d transition state					5o	5o → 6d transition state				
R	ΔG	ΔG‡	Pd–N	Pd–O	Pd–C	dihe	ΔG	ΔG‡	Pd–N	Pd–O	Pd–C	dihe	ΔG	ΔG‡	Pd–N	Pd–O	Pd–C	dihe
t-Bu	−0.2	+11.3	2.44	2.18	2.15	+159	+1.6	+13.0	2.48	2.17	2.14	−152	+1.4	+14.1	2.49	2.16	2.15	−129
Me	+0.2	+14.4	2.37	2.20	2.13	+160	+1.8	+15.9	2.35	2.21	2.13	−155	+2.1	+13.6	2.35	2.20	2.13	−127
H	−0.3	+13.1	2.35	2.20	2.13	+152	+0.7	+13.1	2.33	2.21	2.13	−160	+0.9	+12.4	2.33	2.21	2.13	−131

[a]The solvation free energies of the starting structures (kcal/mol), solvation free energies of activation (kcal/mol), bond distances (Å), and the dihedral angles (deg) for the reductive C–C coupling transition state are given at 25 °C.

Table 1. Summary of Data for the Reductive Coupling of 5x → 7d, 5p → 6d, and 5o → 6d for Complexes with R = t-Bu, Me, H[a]

It is important to point out that, for the t-Bu series, the coupling that begins from 5o has a higher barrier than coupling from 5p and that there is a major difference in the dihedral angle at the transition state for the allyl (reflecting that rotating the enolate down also rotates the allyl group down away from the t-Bu group); relieving the steric strain between the CH2 of the enolate and the t-Bu group of the ligand does not result in the expected stabilization. This may be attributed to the observation that the enolate has to move up from its optimal binding orientation to reach the allyl for the coupling and thus ends up between the two optimal binding orientations for the enolate oxygen binding to the palladium.

The second observation is that the Pd–N bond shortens for all three transition states as the R group is reduced in size from t-Bu to Me to H. This is primarily determined not by the steric interactions between the ligand and the substrates but by the steric interactions between the axial phenyl of the diphenylphosphino ligand and the R group, which pushes the oxazoline N away from the palladium. There is a concomitant lengthening of the Pd–O bond of the enolate, which results in increased electron density at the enolate carbon, facilitating the C–C bond formation.

Third, the transition state for this exothermic step is relatively early, and the preference of Pd(II) is to bind an alkene at a 90° angle relative to the plane formed by the ligands. The transition state of the coupling, to the degree it resembles Pd(II), would prefer the forming alkene of the product to be as close to 90° as possible. This factor selectively stabilizes the transition states for the 5o → 6d couplings relative to the other two beginning from 5p and 5x.

The overall ranking of the free energies of activation is based on the interplay of these factors. On consideration of the experimental system (t-Bu), the relatively long Pd–N bond for all three transition states and the deviation from the ideal Pd–O–C bond angles of the enolate for 5o result in the order observed, in which 5x → 7d is the best balance of factors, 5p → 6d is disfavored relative to 5x → 7d by the steric interaction of the enolate CH2 with the t-Bu, and 5o → 6d is disfavored by the previously cited deviation from one of the two ideal enolate binding angles. Changing to the smaller Me group shortens the Pd–N bond for all three transition states, which improves the nucleophilicity of the enolate for all three couplings but counterintuitively increases the steric interaction of the forming ketone with the ligand (note that shortening the Pd–N bond coincides with the switch to a trigonal geometry for the product), destabilizing 5x → 7d and 5p → 6d relative to 5o → 6d, the last of which is also stabilized relative to the other two by the preferred dihedral angle (i.e., closest to 90°). Finally, with R = H, relieving the steric strain relative to the Me brings the activation energies down and the removal of the steric interaction of the enolate CH2 with the ligand leads to convergence of the pathways and enantioselection is lost. Note that 5o → 6d, with its preferred dihedral, is now the lowest energy pathway.(33)

A brief study of the effect of the methods used in the calculations is summarized in Table 2, which lists alternative methods used to examine the barrier heights for the 5x → 7d and 5p → 6d reductive coupling steps. Within this limited range of methods explored, the barrier leading to

the S enantiomer was consistently lower in energy than that to the R enantiomer. Although some of the calculated barriers are lower and some higher than that required to account for the 89% ee (coinciding with a $\Delta\Delta G‡$ = 1.7 kcal/mol at 24 °C), the results consistently favor the formation of the S enantiomer and thereby support the mechanism. That the results are not only internally consistent across methods but also agree with experimental results gives us confidence that they are meaningful.

Table 2. Difference in the Free Energies of Activation and the Solvation Free Energies of Activation Calculated for the 5x → 7d and 5p → 6d Reductive Coupling Steps at Various Levels of Theory

functional	basis set	solvation	$\Delta\Delta G^‡$	SMD $\Delta\Delta G^‡$
b3lyp	6-31g*	pcm, THF	1.5	1.7
b3lyp	6-31g*	COSMO, THF	3.6	3.6
b3lyp	6-31g*	pcm, water	1.1	1.2
m062x	6-31g*	pcm, THF	0.7	0.8
b3lyp	6-31g*	none	1.1	N/A
b3lyp	6-31+g**	pcm, THF	1.0	1.2

[a] All values favor the S enantiomer and are given in kcal/mol at 25 °C.

Considering that the stated goal at the outset of this work was to provide a comprehensive analysis of the reaction mechanism for the specific Tsuji–Trost allylic alkylation reaction, it was important for us to re-examine the outer-sphere pathway that has been part of the canon for decades.(34) Complex 9, calculated in the solvent continuum model, can proceed via outer-sphere attack (step h, Scheme 2) on the η3-allyl complex to generate 6 and 7 without differentiation, consistent with the finding of Goddard and Stoltz that the outer-sphere mechanism is incompatible with the experimental findings and does not account for the enantioselection observed.(15,16) However, this treatment of 9 is approximate, at best, particularly considering that modeling reaction steps that either generate an ion pair (e.g., the oxidative addition step yielding a cationic palladium complex and the anionic enolate) or recombine existing ions (e.g., the outer-sphere reductive coupling) are problematic with regard to solvation models.(35) Without a solvation model, the separated ion pair's electrostatic attraction is significantly overestimated and results in an artificially low barrier due to the exothermicity of the recombination. To this end, we emulated a successful approach from others(36,37) that modeled the outer-sphere recombination step by including an explicit metal ion (lithium bound to two THF molecules, in our case) as an escort for the anionic nucleophile. Use of a lithium enolate has longstanding precedence from experiment;(38) the resulting neutral nucleophile would approximate the potential involvement of a bimetallic complex and addresses the issue of nucleophilic attack by an unstabilized enolate being so exothermic that little facial discrimination would be possible.

Twenty-four pathways of outer-sphere approach were defined between the enolate and the Pd-η3-allyl by virtue of the four key modes of differentiation illustrated in Figure 5: (a) the exo vs endo orientation of the η3-allyl, (b) the Re vs Si prochiral face of the enolate (which yield S and R enantiomeric C–C coupled products with the allyl, respectively), (c) the nucleophilic attack at the allyl carbon that is proximal vs distal to the chiral oxazoline ring, and (d) the three staggered orientations of the enolate, defined by the relative orientation of the allyl and the unsaturated bond of the enolate. All 2 × 2 × 2 × 3 combinations of approach for the outer-sphere

reductive coupling pathways were examined with NEB/dimer calculations, and all of them were conducted in the presence of Li+·2THF coordinated to the enolate for the reasons stated above. A summary of the results is presented in Table 3.

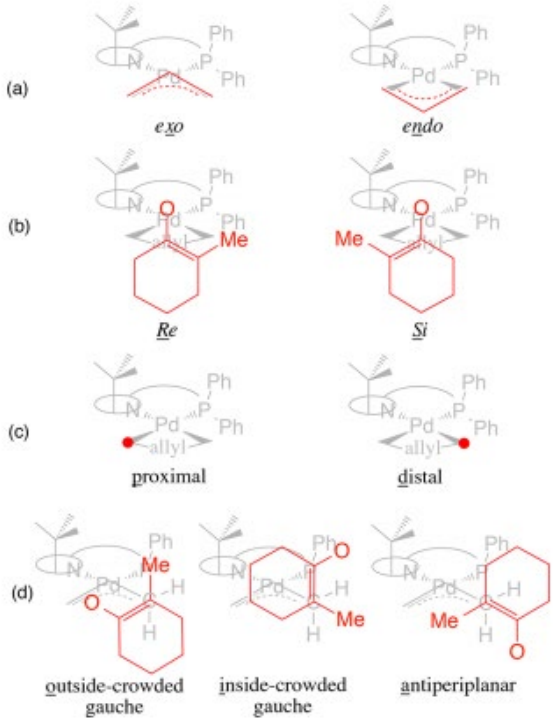

Figure 5. Fundamental features of outer-sphere attack that give rise to the 24 distinctly different pathways (2 × 2 × 2 × 3) including (a) exo vs endo allyl orientation, (b) Re vs Si presentation of the prochiral enolate, (c) formation of the C−C bond at the allyl carbon that is proximal vs distal to the chiral oxazoline ring, and (d) three rotational orientations of the enolate relative to the sp2-hybridized allyl carbon to which it will bind. Note that the exo allyl and Re enolate orientations depicted in (d) were arbitrarily chosen for the sake of illustration. One-letter designations for each component of the path are underlined, the various combinations of which are used in Table 3.

Table 3. Relative Solvation Free Energies of the C−C Coupled Products and Solvation Free Energies of Activation Leading to Their Formation, in kcal/mol, for the 24 Outer-Sphere Reductive Coupling Pathways Defined by 2 × 2 × 2 × 3 Combinations Shown in Figure 5a

yields *S* product **7**			yields *R* product **6**		
path	$\Delta G^{\ddagger}$	ΔG	path	$\Delta G^{\ddagger}$	ΔG
xRpa	+10.2	−11.2	xSpa	+11.0	−12.6
i	+9.2	−8.9	i	+11.4	−9.0
o	+10.1	−13.7	o	+6.9	−13.3
xRda	+11.9	−10.8	xSda	+10.3	−11.4
i	+15.3	−9.3	i	+13.5	−7.6
o	+11.6	−13.0	o	+9.5	−11.8
nRpa	+7.8	−11.0	nSpa	+9.1	−10.6
i	+8.0	−9.3	i	+8.9	−10.5
o	+7.6	−10.9	o	+9.3	−10.2
nRda	+8.9	−12.0	nSda	+10.4	−13.1
i	+11.3	−10.4	i	+14.8	−8.5
o	+10.4	−13.6	o	+10.5	−13.9

[a]The energetic baseline is the Li^{+}·2THF derivative of **9**.

It is important to highlight that in the outer-sphere mechanism, structure 9, which is formed following the irreversible decarboxylation of 2, cannot easily be placed on the same energy surface as the step that preceded it. The same can be said for the transition between 4 and 5 for the inner-sphere mechanism. We find it extremely difficult to capture all components of the energy in dissociation/association steps and, as such, feel that a different energetic manifold—with its own baseline—begins at this point along the reaction pathway. For the outer-sphere mechanism considered here, the most sensible choice for the new baseline at 9 seemed to be the derivative of lowest energy. While all of the species of 9 were close in energy, those that were lowest had the exo orientation of the allyl. Importantly, although the solvation free energies of activation given in Table 3 have values lower than those shown in Figure 3 for the inner-sphere C–C coupling step, this is a consequence of the chosen baseline, which, as we stated previously, is different between the two. It is reasonable to expect that 9, a species with separated charge, is higher in energy than 1, the species used as the baseline in the comparative energy diagrams within this work, and that the associated outer-sphere barriers could easily be higher than those for inner sphere.

Close examination of the values in Table 3 reveals that the lowest barrier (+6.9 kcal/mol above the reference) to outer-sphere reductive C–C coupling comes from the xSpo pathway and results in an R enantiomer, in contrast to what is observed experimentally. Even if this barrier is considered spurious, the next three barriers above it (nRpo, nRPa, and nRpi are +7.6, + 7.8, and +8.0 kcal/mol above the reference) favor the S enantiomer, and then nSpi is just above them at +8.9 kcal/mol, again favoring the R enantiomer. This ensemble clearly indicates poor selectivity and reflects the approach of the nucleophile to the coordinated allyl on a trajectory that results in little selectivity (vide infra). One might think that these outer-sphere barrier energies would reflect the stability of the product, but that is clearly not the case according to the data shown in Table 3. Asymmetric induction, in this case, requires some kind of interaction between the enolate and the chiral t-Bu-phox ligand.As illustrated in the side view of Figure 6, considerable spatial separation exists between the prochiral enolate nucleophile and the chiral metal allyl. Such separation makes it unlikely that the outer-sphere mechanism can impart enantiodiscrimination. Other ligands designed for decarboxylative asymmetric allylic alkylation reactions,(39) such as the popular L4 ligand,(40) create an obvious chiral pocket near the allyl that can impart asymmetric induction. As a recent report suggests,(41) close spatial proximity of the approaching nucleophile to the electrophile is required in order to achieve the kind of hydrogen-bonding direction between an amide proton of the L4 ligand and the enolate oxygen. Such direction by hydrogen bonding in outer-sphere mechanisms has been proposed for other systems.(36)

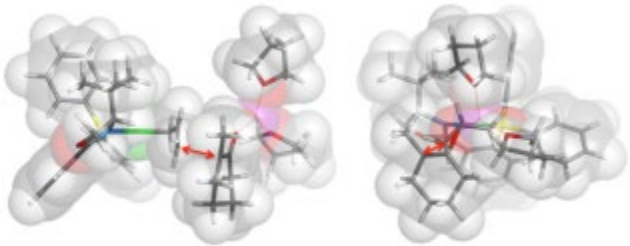

Figure 6. Two views of the transition state for the lowest-energy pathway to outer-sphere coupling between Pd-η1-allyl and enolate (Li+·2THF). This step coincides with the exo, Si, proximal, outside-crowded gauche approach vector (xSpo) defined in Figure 5. The red arrow highlights the atoms involved in C−C coupling.

Finally, two pathways evolve from complex 2 that involve recombination of the anion with the cationic palladium center (see Scheme 2), and it is these equilibria that manifest the critical role water plays in the catalytic cycle. The lower energy path, (b), has a barrier that is +6.0 kcal/mol relative to baseline and binds the carboxylate to form 3, while the other path, (c), is +14.1 kcal/mol relative to baseline and binds the ketone to form 4. Complex 3 (−3.6 kcal/mol) is significantly more stable than complex 4(+8.6 kcal/mol) and was identified as the resting state of the catalyst in an earlier report.(2) Complex 3 was also reported to be difficult to isolate and was crystallographically characterized only after extensive effort and purification.(2) The computational modeling supports the stability of complex 3; as discussed above, it is 12.2 kcal/mol more stable than 4. However, the addition of one or two explicit molecules of water to these complexes reduces the energy difference by 2.0 and 7.4 kcal/mol, respectively, as the stability from hydrogen bonding to the carboxylate is preferential in 4 relative to 3, as shown in Figure 7.(42) In addition to the significant shift in the equilibrium concentration of 4 relative to that of 3, it is expected that, as complex 4 is preferentially stabilized by the presence of water, the corresponding transition state would also become more stable, according to the Hammond postulate.(43) The original report stated, “Interestingly, impure samples of <3> visibly expelled a gas (presumably CO2) in the solid state and effervesced in solution.”(2) The impurities most likely referred to trace water and the water-stabilized 4, which readily decarboxylates (vide infra). In the absence of water, structure 3 predominates, but this structure does not readily decarboxylate.

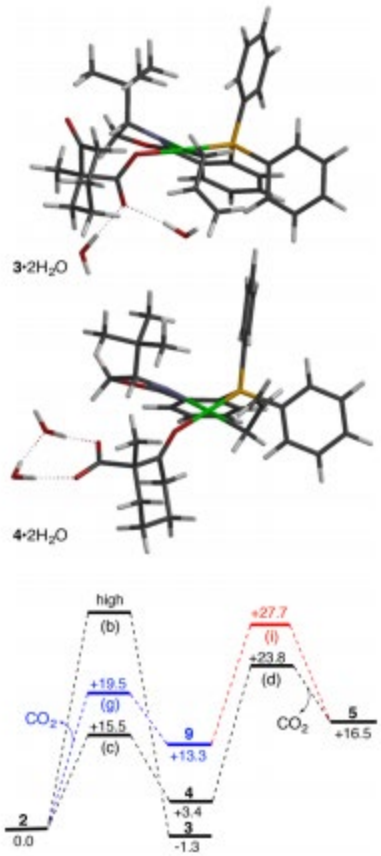

Figure 7. (top) Lowest energy calculated molecular structures of 3·2H2O and 4·2H2O. The solvation free energy difference between 3 and 4 is reduced from 12.2 kcal/mol in the absence of explicit water to 4.7 kcal/mol for the double hydrate. (bottom) Revised energy diagram for the transformation of 2 to 5 in the presence of two explicit water molecules.

Even if the transition state were not lowered in energy by the coordination of the water, calculations show that decarboxylation from 4 can occur readily (+13.4 above baseline; Scheme 2, step (d)), generating 5 directly. Complex 2 can also decarboxylate to form complex 9 (step g), but the calculated pathway is significantly higher in energy with a transition state +20.4 kcal/mol above baseline, and 9 itself is +19.2 kcal above the baseline. This preference for the metal-mediated decarboxylation pathway is reversed from that found in a related study of the decarboxylation of α-(diphenylmethylene) imino esters.(44) As that decarboxylation involves formation of a 2-azaallyl anion initially coordinated through the nitrogen that subsequently rearranges to the carbon-coordinated species, it is not clear how comparable those results are to the direct formation of the coordinated enolate complex formed directly in this study. Complex 9 can rearrange directly to 5 with a barrier of 20.5 kcal (step i) or indirectly via 10 (steps j and k) with lower barriers.

A modified energy scheme for the conversion of 2 to 5 in the presence of two explicit molecules of water is shown in Figure 7. While the results provide insight into a possible mechanism for water to affect the energetics of the decarboxylation, it is important to note that significant uncertainty exists due to the extremely complex nature of the calculations.(45,46) By their very definition, the hydrogen-bonded interactions are soft and the NEB and dimer calculations that follow the reaction energy path are much less well behaved. Additional

uncertainty derives from the loosely held dissociated fragments (H2O and CO2) in the products and casts doubt on whether the rotational/translational contribution to the entropy is fully captured. With two explicit waters in the calculation, no single-step direct interconversion between 2 and 3 could be found. Clearly, this step involves more complex motion possibly involving dissociation of one or both waters from the charged fragments, η3- to η1-allyl rearrangement, coordination of one of the oxygens of the carboxylate, and association of the waters. Unsurprisingly, the direct path maintained a very high barrier (shown in Figure 7, step b) even after thousands of NEB cycles. That a direct interconversion pathway between decarboxylated ion pair complex 9 and 5 was found (vide supra) emphasizes the current level of unpredictability involved in mapping these very complex steps and warrants additional study.

An overall view of the calculated energetics for the key steps in the asymmetric Tsuji–Trost decarboxylative allylation reaction is summarized in Figure 8. In the first part of the reaction, oxidative addition (a) is the slow step. The presence of water preferentially stabilizes 4 relative to 3 in the ligand recombination steps (b) and (c), and this preferential stabilization is crucial for the subsequent decarboxylation step (d), as it may only proceed from 4. Facile interconversion (e) among the PdII-η1-allyl-enolate conformers sets the stage for enantioselective reductive C–C coupling (f), which, as discussed above, consistently favors formation of the S enantiomer, in agreement with the experimental findings.

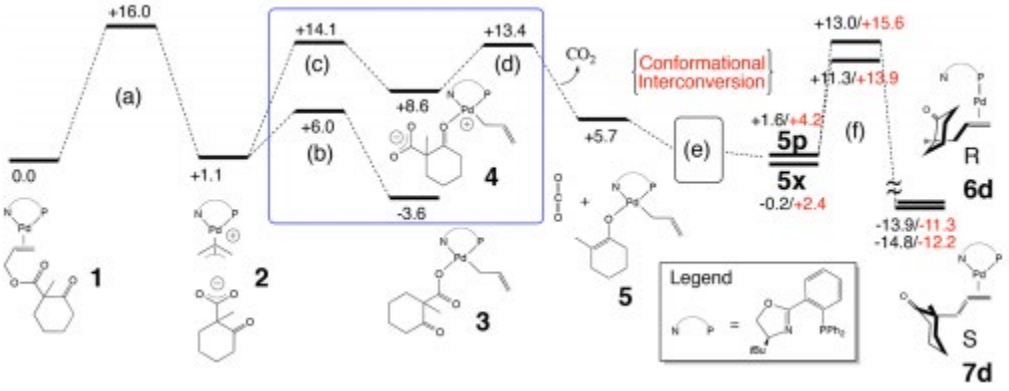

Figure 8. Calculated potential energy surface for the primary steps in the Tsuji−Trost allylation reaction. Numbers depict solvation free energies (for the mimina) or solvation free energies of activation (for the transition states), and are reported in kcal/mol relative to 1 for the steps leading up to 5 and relative to 1 (black) and 5k (red) for those that follow. Structures shown within the blue box are affected by the presence of explicit waters. Conformational interconversion as illustrated in Figure 2 is implied in the black box at (e). Steps (a)−(f) correspond to those shown in Scheme 2.

Conclusion

DFT and NEB computational methods have been used to construct a multistep mechanism that is consistent with experimental data for the palladium-catalyzed asymmetric Tsuji–Trost decarboxylative allylation reaction. Two key facets of the reaction are the efficiency and enantioselectivity of the process. This study clarifies several previously unexplained aspects of the mechanism. A plausible low-energy interconversion pathway for the various conformers of 5, a square-planar PdII-η1-allyl-enolate intermediate, has been constructed that emphasizes

how enantioselection must emanate from a subsequent step—in this case, that of reductive C–C coupling. Due to the highly asynchronous nature of the coupling step, we have introduced a new approach utilizing a two-part NEB guess that allowed significantly more rapid location of the transition states while retaining certainty about the accuracy of the stationary point. Barrier heights for the formation of the S enantiomer were consistently lower in energy than those found for the formation of the corresponding R enantiomer and were found to be due primarily to the interaction of the enolate CH2 with the t-Bu. Truncation of the R group of the ligand from t-Bu to Me to H elucidated the important roles of the axial diphenylphosphino phenyl group of the ligand interacting with the R group to determine the Pd–N and Pd–O bond lengths, the P–Pd–C–C dihedral angle of the allyl group, and the angle of the enolate binding to the palladium on the enantioselection. For the lowest energy S and R pathways, several levels of theory that involved changes in density functional, basis set, and solvation model were used to re-examine the steps, and all supported the energetic preference of the S pathway, which is consistent with experiment.

Further, a detailed analysis of the outer-sphere mechanism was conducted in the presence of a metal cation escort. From a global perspective, the multiple pathways examined failed to reveal clear discrimination in the formation of the two enantiomeric products. Close examination of the pathways revealed that the lowest energy route resulted in the formation of the wrong (R) enantiomer.

Water was found to play a potentially critical role in the preferential stabilization of the ketone-bound complex 4 relative to the carboxylate-bound 3, which is known to be the resting state of the cycle. Importantly, complex 3 does not readily decarboxylate and therefore does not reside on the catalytic cycle itself, whereas complex 4 readily undergoes decarboxylation to produce the essential precursor to reductive C–C coupling, the four-coordinate square-planar Pd(II)-η1-allyl-enolate structure 5. Decarboxylation of 4 also leads directly to structure 5 and circumvents the need for the relatively high energy five-coordinate square-pyramidal PdII-η3-allyl-enolate complex 10 as the purported intermediate required for the enantioselective rearrangement that generated 5.

Associated content

Supporting Information

The Supporting Information is available free of charge on the ACS Publications website at DOI: 10.1021/acs.organomet.8b00507.

Expansion of Figure 3 from the main text and figure for ref 33 from the main text (PDF)

Cartesian coordinates, solvation free energies, and solvation free energies of activation (relative to baseline complex 1, in kcal/mol, and absolute values, in hartrees) of all complexes reported herein (XYZ)

Author information

Corresponding Authors

*E-mail for A.T.M.: moreheada@ecu.edu.

*E-mail for A.L.S.: sargenta@ecu.edu.

ORCID

Mitchell P. Croatt: 0000-0002-5643-7215

Andrew T. Morehead, Jr.: 0000-0001-7812-4773
Andrew L. Sargent: 0000-0002-5758-8787

Notes

The authors declare no competing financial interest.

Acknowledgments

East Carolina University and the National Science Foundation (CHE-0415484, A.T.M.; CNS-0619285, A.L.S.) are gratefully acknowledged for their support of this work. Funding from the North Carolina Biotechnology Center (BRG-1205) for M.P.C. is gratefully acknowledged.

References

(1) Ojima, I. In Catalytic Asymmetric Synthesis, 3rd ed.; Wiley: New York, 2010.
(2) Sherden, N. H.; Behenna, D. C.; Virgil, S. C.; Stoltz, B. M. Unusual Allylpalladium Carboxylate Complexes: Identification of the Resting State of Catalytic Enantioselective Decarboxylative Allylic Alkylation Reactions of Ketones. Angew. Chem., Int. Ed. 2009, 48, 6840−6843.
(3) Weaver, J. D.; Recio, A., III; Grenning, A. J.; Tunge, J. A. Transition Metal-Catalyzed Decarboxylative Allylation and Benzylation Reactions. Chem. Rev. 2011, 111, 1846−1913.
(4) Yoshimura, T. Catalytic Asymmetric Reactions in Alkaloid and Terpenoid Syntheses. Tetrahedron Lett. 2014, 55, 5109−5118.
(5) Wender, P. A.; Verma, V. A.; Paxton, T. J.; Pillow, T. H. FunctionOriented Synthesis, Step Economy, and Drug Design. Acc. Chem. Res. 2008, 41, 40−49.
(6) White, D. E.; Stewart, I. C.; Grubbs, R. H.; Stoltz, B. M. The Catalytic Asymmetric Total Synthesis of Elatol. J. Am. Chem. Soc. 2008, 130, 810−811.
(7) Brookes, P. A.; Cordes, J.; White, A. J. P.; Barrett, A. G. M. Total Synthesis of Mycophenolic Acid by a Palladium-Catalyzed Decarboxylative Allylation and Biomimetic Aromatization Sequence. Eur. J. Org. Chem. 2013, 2013, 7313−7319.
(8) Shen, X.-L.; Zhao, R.-R.; Mo, M.-J.; Peng, F.-Z.; Zhang, H.-B.; Shao, Z.-H. Catalytic Enantioselective and Divergent Total Synthesis of (+)-10-Oxocylindrocarpidine, (+)-Cylindrocarpidine, (−)-N-Acetylcylindrocarpinol, and (+)-Aspidospermine. J. Org. Chem. 2014, 79, 2473−2480.
(9) Li, Z.; Zhang, S.; Wu, S.; Shen, X.; Zou, L.; Wang, F.; Li, W.; Peng, F.; Zhang, H.; Shao, Z. Enantioselective Palladium-Catalyzed Decarboxylative Allylation of Carbazolones: Total Synthesis of (−)-Aspidospermidine and (+)-Kopsihainanine A. Angew. Chem., Int. Ed. 2013, 52, 4117−4121.
(10) Horeischi, F.; Biber, N.; Plietker, B. The Total Synthesis of Guttiferone A and 6-epi-GuttiferoneA. J. Am. Chem. Soc. 2014, 136, 4026−4030.
(11) Ghosh, S.; Chaudhuri, S.; Bisai, A. Catalytic Enantioselective Decarboxylative Allylations of a Mixture of Allyl Carbonates and Allyl Esters: Total Synthesis of (−)- and (+)-Folicanthine. Chem. - Eur. J. 2015, 21, 17479−17484.
(12) Pappoppula, M.; Aponick, A. Enantioselective Total Synthesis of (−)-Martinellic Acid. Angew. Chem., Int. Ed. 2015, 54, 15827−15830.

(13) Leng, L.; Zhou, X.; Liao, Q.; Wang, F.; Song, H.; Zhang, D.; Liu, X.-Y.; Qin, Y. Asymmetric Total Synthesis of Kopsia Indole Alkaloids. Angew. Chem., Int. Ed. 2017, 56, 3703−3707.
(14) (a) Johansson, C.; Lloyd-Jones, G. C.; Norrby, P.-O. Memory and Dynamics in Pd-Catalyzed Allylic Alkylation with P,N-Ligands. Tetrahedron: Asymmetry 2010, 21, 1585−1592. (b) Fristrup, P.; Jensen, T.; Hoppe, J.; Norrby, P.-O. Deconvoluting the Memory Effect in PdCatalyzed Allylic Alkylation: Effect of Leaving Group and Added Chloride. Chem. - Eur. J. 2006, 12, 5352−5360.
(15) Keith, J. A.; Behenna, D. C.; Mohr, J. T.; Ma, S.; Marinescu, S. C.; Oxgaard, J.; Stoltz, B. M.; Goddard, W. A., III The Inner-Sphere Process in the Enantioselective Tsuji Allylation Reaction with (S)-t-Buphosphinooxazoline Ligands. J. Am. Chem. Soc. 2007, 129, 11876−11877.
(16) Keith, J. A.; Behenna, D. C.; Sherden, N.; Mohr, J. T.; Ma, S.; Marinescu, S. C.; Nielsen, R. J.; Oxgaard, J.; Stoltz, B. M.; Goddard, W. A., III The Reaction Mechanism of the Enantioselective Tsuji Allylation: Inner-Sphere and Outer-Sphere Pathways, Internal Rearrangements, and Asymmetric C-C Bond Formation. J. Am. Chem. Soc. 2012, 134, 19050−19060.
(17) McPherson, K. E.; Bartolotti, L. J.; Morehead, A. T., Jr.; Sargent, A. L. Utility of the Nudged Elastic Band Method in Identifying the Minimum Energy Path of an Elementary Organometallic Reaction Step. Organometallics 2016, 35, 1861−1865.
(18) Frisch, M. J.; Trucks, G. W.; Schlegel, H. B.; Scuseria, G. E.; Robb, M. A.; Cheeseman, J. R.; Scalmani, G.; Barone, V.; Mennucci, B.; Petersson, G. A.; Nakatsuji, H.; Caricato, M.; Li, X.; Hratchian, H. P.; Izmaylov, A. F.; Bloino, J.; Zheng, G.; Sonnenberg, J. L.; Hada, M.; Ehara, M.; Toyota, K.; Fukuda, R.; Hasegawa, J.; Ishida, M.; Nakajima, T.; Honda, Y.; Kitao, O.; Nakai, H.; Vreven, T.; Montgomery, J. A., Jr.; Peralta, J. E.; Ogliaro, F.; Bearpark, M.; Heyd, J. J.; Brothers, E.; Kudin, K. N.; Staroverov, V. N.; Keith, T.; Kobayashi, R.; Normand, J.; Raghavachari, K.; Rendell, A.; Burant, J. C.; Iyengar, S. S.; Tomasi, J.; Cossi, M.; Rega, N.; Millam, J. M.; Klene, M.; Knox, J. E.; Cross, J. B.; Bakken, V.; Adamo, C.; Jaramillo, J.; Gomperts, R.; Stratmann, R. E.; Yazyev, O.; Austin, A. J.; Cammi, R.; Pomelli, C.; Ochterski, J. W.; Martin, R. L.; Morokuma, K.; Zakrzewski, V. G.; Voth, G. A.; Salvador, P.; Dannenberg, J. J.; Dapprich, S.; Daniels, A. D.; Farkas, O.; Foresman, J. B.; Ortiz, J. V.; Cioslowski, J.; Fox, D. J. Gaussian 09, Revision D.01; Gaussian, Inc., Wallingford, CT, 2013.
(19) Alfonso, D. R.; Jordan, K. D. A Flexible Nudged Elastic Band Program for Optimization of Minimum Energy Pathways Using Ab Initio Electronic Structure Methods. J. Comput. Chem. 2003, 24, 990− 996.
(20) Henkelman, G.; Jonsson, J. A Dimer Method for Finding Saddle´ Points on High Dimensional Potential Surfaces Using Only First Derivatives. J. Chem. Phys. 1999, 111, 7010−7022.
(21) Heyden, A.; Bell, A. T.; Keil, F. J. Efficient Methods for Finding Transition States in Chemical Reactions: Comparison of Improved Dimer Method and Partitioned Rational Function Optimization Method. J. Chem. Phys. 2005, 123, 224101−224114.
(22) Becke, A. D. Density-Functional Thermochemistry. III. The Role of Exact Exchange. J. Chem. Phys. 1993, 98, 5648−5652.

(23) Lee, C.; Yang, W.; Parr, R. G. Development of the Colle-Salvetti Correlation-Energy Formula into a Functional of the Electron Density. Phys. Rev. B: Condens. Matter Mater. Phys. 1988, 37, 785−789.
(24) Andrae, D.; Haeussermann, U.; Dolg, M.; Stoll, H.; Preuss, H.¨Energy-Adjusted Ab Initio Pseudopotentials for the Second and Third Row Transition Elements. Theor. Chim. Acta 1990, 77, 123−141.
(25) Miertus, S.; Scrocco, E.; Tomasi, J. Electrostatic Interactions of a Solute With a Continuum. A Direct Utilization of Ab Initio Molecular Potentials for the Prevision of Solvent Effects. Chem. Phys. 1981, 55, 117−129.
(26) Miertus, S.; Tomasi, J. Approximate Evaluations of the Electrostatic Free Energy and Internal Energy Changes in Solution Processes. Chem. Phys. 1982, 65, 239−245.
(27) (a) Marenich, A. V.; Cramer, C. J.; Truhlar, D. G. Performance of SM6, SM8, and SMD on the SAMPL1 Test Set for the Prediction of Small-Molecule Solvation Free Energies. J. Phys. Chem. B 2009, 113, 6378−6396. (b) Marenich, A. V.; Cramer, C. J.; Truhlar, D. G. Universal Solvation Model Based on Solute Electron Density and on a Continuum Model of the Solvent Defined by the Bulk Dielectric Constant and Atomic Surface Tensions. J. Phys. Chem. B 2009, 113, 6378−6396.
(28) Henkelman, G.; Uberuaga, B. P.; Jonsson, H. A Climbing Image´ Nudged Elastic Band Method for Finding Saddle Points and Minimum Energy Paths. J. Chem. Phys. 2000, 113, 9901−9904.
(29) Zhao, Y.; Truhlar, D. G. The M06 Suite of Density Functionals for Main Group Thermochemistry, Thermochemical Kinetics, Noncovalent Interactions, Excited States, and Transition Elements: Two New Functionals and Systematic Testing for Four M06-class Functionals and 12 Other Functionals. Theor. Chem. Acc. 2008, 120, 215−241.
(30) Klamt, A. Conductor-like Screening Model for Real Solvents: A New Approach to the Quantitative Calculation of Solvation Phenomena. J. Phys. Chem. 1995, 99, 2224−2235.
(31) Klamt, A.; Jonas, V. Treatment of the Outlying Charge in Continuum Solvation Models. J. Chem. Phys. 1996, 105, 9972−9981.
(32) Klamt, A.; Schueuermann, G. COSMO: A New Approach to Dielectric Screening in Solvents with Explicit Expressions for the Screening Energy and its Gradient. J. Chem. Soc., Perkin Trans. 2 1993, 2, 799−805.
(33) Reductive C−C coupling calculations where the allyl and enolate have swapped positions were performed, but with dramatically higher barriers. See the Supporting Information.
(34) Trost, B. M.; Verhoeven, T. R. Allylic Substitutions with Retention of Stereochemistry. J. Org. Chem. 1976, 41, 3215−3216.
(35) Deglmann, P.; Schenk, S. Theremodynamics of Chemical Reactions with COSMO-RS: The Extreme Case of Charge Separation or Recombination. J. Comput. Chem. 2012, 33, 1304−1320.
(36) Butts, C. P.; Filali, E.; Lloyd-Jones, G. C.; Norrby, P.-O.; Sale, D. A.; Schramm, Y. J. Am. Chem. Soc. 2009, 131, 9945−9957.
(37) Chen, J.-P.; Peng, Q.; Lei, B.-L.; Hou, X.-L.; Wu, Y.-D. Chemoand Regioselectivity-Tunable Pd-Catalyzed Allylic Alkylation of Imines. J. Am. Chem. Soc. 2011, 133, 14180−14183.

(38) Trost, B. M.; Self, C. R. On the Palladium-Catalyzed Alkylation of Silyl-Substituted Allyl Acetates with Enolates. J. Org. Chem. 1984, 49, 468−473.
(39) Trost, B. M.; Van Vranken, D. L. Asymmetric Ligands for Transition-Metal-Catalyzed Reactions: 2-Diphenylphosphinobenzoyl Derivatives of C2-Symmetric Diols and Diamines. Angew. Chem., Int. Ed. Engl. 1992, 31, 228−230.
(40) Trost, B. M.; Xu, J.; Schmidt, T. Palladium-Catalyzed Decarboxylative Asymmetric Allylic Alkylation of Enol Carbonates. J. Am. Chem. Soc. 2009, 131, 18343−18357.
(41) Jackson, M.; O'Broin, C. Q.; Müller-Bunz, H.; Guiry, P. J. Enantioselective Synthesis of Sterically Hindered α-allyl-α-aryl Oxindoles via Palladium-Catalyzed Decarboxylative Asymmetric Allylic Alkylation. Org. Biomol. Chem. 2017, 15, 8166−8178.
(42) Numerous isomers of the hydrated complexes were evaluated, and the lowest energies were attained when the waters interacted with the oxygen atoms of the carboxylate and not with the ketone oxygen.
(43) Hammond, G. S. A. Correlation of Reaction Rates. J. Am. Chem. Soc. 1955, 77, 334−338.
(44) Li, Z.; Jiang, Y.-Y.; Yeagley, A. A.; Bour, J. P.; Liu, L.; Chruma, J. J.; Fu, Y. Mechanism of the Pd-Catalyzed Decarboxylative Allylation of a-Imino Esters: Decarboxylation via Free Carboxylate Ion. Chem. - Eur. J. 2012, 18, 14527−14538.
(45) Great variability exists in calculating entropy corrections to the solvation free energies. See, for example: Plata, R. E.; Singleton, D. A. A Case Study of the Mechanism of Alcohol-Mediated Morita BaylisHillman Reactions. The Importance of Experimental Observations. J. Am. Chem. Soc. 2015, 137, 3811−3826. There is little consensus regarding a best means to redress the error. Our treatment aims to simply gauge the impact of added solute in a relative manner.
(46) Hagelin, H.; Åkermark, B.; Norrby, P.-O. A Solvated Transition State for the Nucleophilic Attack on Cationic η^3-Allylpalladium Complexes. Chem. - Eur. J. 1999, 5, 902−909.